J Eng Math (2020) 121:125–139
https://doi.org/10.1007/s10665-020-10044-9

Antiplane response of a flat-bottomed semicircular canyon to cylindrical elastic waves

Kao-Hao Chang · Wei-Chien Wang · Shan-Chung Hsu

Received: 24 July 2019 / Accepted: 13 March 2020 / Published online: 7 April 2020

Abstract The purpose of this study is to theoretically probe how the joint effects of near-field source and surface topography impact the seismic wavefields. A simplified canyon model, which couples a semicircular model with a model for minor segments, is used to predict characteristic changes in ground motions due to line-source excitation. Based on a semi-analytical procedure using the region-matching technique, a Fourier–Bessel series solution is derived. Distinct coordinate systems are unified with the aid of Graf's addition formula. Comparisons with boundary-element solutions verify the modelling framework proposed. Steady-state and transient simulations are both conducted.

Keywords Near-source effect · Scattering · Topographic effect · Wavefunction

1 Introduction

Topographic irregularities have long been recognized as one of the essential elements in affecting the shaking levels associated with earthquakes. Hence, the so-called *topographic effect* (i.e. interaction between incoming seismic waves and geomorphic features) may become crucial in many researches pertinent to earthquake engineering and engineering seismology (e.g. [1]).

Generally, theoretical schemes are feasible for simple geometrical shapes only, the two-dimensional (2-D) ones in particular. Exact analytical solutions (see [2,3]) may be derived via the method of separation of variables (MSV), commonly called in elastodynamics the method of wavefunction expansions. For some simple geometries that the MSV fails to work, the region-matching technique (RMT) offers an opportunity to make the utilization of the MSV

K.-H. Chang (✉) · S.-C. Hsu
Department of Civil Engineering, Chung Yuan Christian University, No. 200, Chung Pei Road, Chung Li District, Taoyuan 32023, Taiwan, Republic of China
e-mail: khchang@cycu.edu.tw

S.-C. Hsu
e-mail: handsomeguy200@163.com

W.-C. Wang
Department of Civil Engineering, National Central University, No. 300, Chung Da Road, Chung Li District, Taoyuan 32001, Taiwan, Republic of China
e-mail: weichien@ncu.edu.tw

possible. Making good use of the RMT usually gives rise to a series solution, which is a good substitute for an exact analytical solution. Over the last few years, the RMT has been applied to deal effectively with a number of problems regarding antiplane scattering [4–10].

So far, comparatively little attention has been given to addressing issues of truncated surficial obstacles. Lately, the problem of the interaction of a flat-bottomed semicircular canyon and incident plane SH waves has been explored by Tsaur and Chang [11]. The 2-D cross-sectional shape of a flat-bottomed semicircular canyon may be deemed as the area remaining after removing a minor segment from a semicircle. Similar topics concerning a flat-bottomed semielliptic canyon may be found in the work of Hsu and Tsaur [12]. As to a shallow V-shaped gorge, its cross-sectional shape might look like the part left after cutting two pieces out of a semicircle (cf. [13,14]). Subsequently, Zhang et al. [15] followed a similar line on domain decomposition (i.e. cutting three pieces out of a semicircle) to examine the problem of antiplane wave scattering from a trapezoidal canyon.

As a starting point for mathematical modelling of 2-D wave scattering, the case of monochromatic plane-wave incidence is investigated frequently. Consequently, there exists a large body of literature, including a wide range of methodologies for theoretical analysis (e.g. [16–29]) and for numerical simulation (e.g. [30–36]), and covering various aspects from topographic/site effect (e.g. [37–42]) to crack/cavity configuration (e.g. [19,21,22,43–50]). Unfortunately, the far-field approximation (based on the plane-wave assumption) is only valid when seismic sources are far enough from scatterers (e.g. [51]). Indeed, actual cases might be far from the simple plane-wave assumption. For example, many microseismic events have been found to be source location dependent (e.g. [52]). Modern multi-story/high-rise buildings subjected to strong near-source ground motions may exhibit unacceptable collapse performance (e.g. [53]). Damage potential may, therefore, be severe for these structures, especially for those located in urban areas (e.g. [54,55]). This has a direct bearing on risk management demands in seismic monitoring and protection systems, technologies adopted, and current best practice.

To take better account of the source-induced near-field contributions, some theoretical models for 2-D cylindrical wave propagation have been devised, such as those for surficial irregularities (e.g. [56,57]), underlying geological structures (e.g. [58–61]), underground obstacles (e.g. [62,63]), and ideal zero-thickness anomalies (e.g. [64]). In addition, to improve practical applicability, several simplified models concerning plane-wave incidence (e.g. [7,10,14,65]) have been further extended to those with line-source excitation (e.g. [66–68]).

Herein, due to the paucity of literature that is available in the context of elastodynamics, the authors aim to investigate the response of a flat-bottomed semicircular canyon subjected to SH cylindrical waves. A Fourier–Bessel series solution is derived, using the RMT along with Graf's addition formula. Taking into account the joint effects of near-field source and surface topography, the characteristics of simulated ground motions will be illuminated later.

2 Theoretical approach

The assumed problem geometry is depicted in Fig. 1, where a flat-bottomed semicircular canyon is considered. This concave topography is characterized by the half-width a and the depth d. The semi-infinite stratum, bounded by the horizontal ground surface, is assumed to be homogeneous, isotropic, and linearly elastic. The first two assumptions are expected to be reasonable for geophysical materials and concrete. The third assumption excludes the effect of attenuation and may be extended to viscoelastic cases in future studies when such an effect becomes more important. The half-plane material has the shear modulus μ and the shear-wave velocity c_s. The intersection of the central axis of the canyon and the horizontal ground surface is taken as the origin of global coordinates (x, y) and (r, θ). The origin of local coordinates (x_1, y_1) and (r_1, θ_1) is set at the midpoint of the bottom surface of the canyon. A line source emitting cylindrical SH waves (with an angular frequency ω) is located at (r_s, θ_s). Assume that in this work, the line source is always located in region 1. We introduce the angular parameter $\pm\beta$ to denote the locations of the endpoints of the flat bottom of the canyon, as shown in Fig. 1. Throughout this section, the time-harmonic regime, with factor $\exp(\mathrm{i}\omega t)$, is assumed.

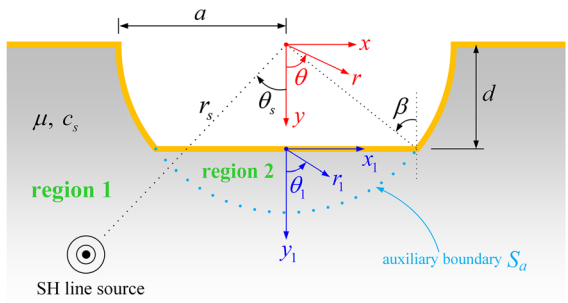

Fig. 1 Geometric layout of the problem. (The parameters are explained in the text.)

Introducing an auxiliary boundary S_a of circular-arc shape, the half plane is divided into two regions: an open region 1 and an enclosed region 2 (see Fig. 1). The steady-state out-of-plane motions in these two regions have to obey

$$\frac{\partial^2 u_j}{\partial r^2}+\frac{1}{r}\frac{\partial u_j}{\partial r}+\frac{1}{r^2}\frac{\partial^2 u_j}{\partial \theta^2}+k^2 u_j=-\frac{\delta(r-r_s)\delta(\theta-\theta_s)}{r},\quad j=1,2, \tag{1}$$

where the subscript j denotes the region number, $k=\omega/c_s$ is the shear wavenumber, and $\delta(\cdot)$ is Dirac's delta function.

The stress-free boundary conditions are imposed on the horizontal ground surface,

$$\tau_{\theta z}^{(1)}=\frac{\mu}{r}\frac{\partial u_1(r,\theta)}{\partial \theta}=0,\quad \theta=\pm\frac{\pi}{2},\quad r>a, \tag{2}$$

on the canyon sides,

$$\tau_{rz}^{(1)}=\mu\frac{\partial u_1(r,\theta)}{\partial r}=0,\quad \beta\le|\theta|\le\frac{\pi}{2},\quad r=a, \tag{3}$$

and at the bottom of the canyon,

$$\tau_{\theta_1 z}^{(2)}=\frac{\mu}{r_1}\frac{\partial u_2(r_1,\theta_1)}{\partial \theta_1}=0,\quad \theta_1=\pm\frac{\pi}{2}. \tag{4}$$

2.1 Wavefunction expressions

For the present boundary-value problem, the use of the method of images is effective. Treating the horizontal ground surface as an ideal mirror, an image of the incident source is introduced. For the half-plane medium without any surface/subsurface anomalies, the free-field displacement u^F may be expressed as a sum of the incident and reflected waves,

$$u^F(r,\theta)=\frac{H_0^{(2)}(k\hat{r})}{H_0^{(2)}(kr_s)}+\frac{H_0^{(2)}(k\tilde{r})}{H_0^{(2)}(kr_s)}, \tag{5}$$

where $H_0^{(2)}(\cdot)$ is the zeroth order Hankel function of the second kind, $\hat{r}$ is the distance from the field point to the wave source, and $\tilde{r}$ is the distance from the field point to the virtual wave source.

We may re-express Eq. (5) in terms of the radial and angular variables of the global coordinate (see e.g. [69]),

$$u^F(r,\theta) = 2\sum_{n=0}^{\infty} \varepsilon_n \frac{H_{2n}^{(2)}(kr_s)}{H_0^{(2)}(kr_s)} \cos(2n\theta_s) J_{2n}(kr) \cos(2n\theta) + 4\sum_{n=0}^{\infty} \frac{H_{2n+1}^{(2)}(kr_s)}{H_0^{(2)}(kr_s)} \sin[(2n+1)\theta_s] J_{2n+1}(kr) \sin[(2n+1)\theta], \tag{6}$$

where ε_n is the Neumann factor (equal to 1 if $n = 0$ and to 2 if $n \geq 1$) and $J_n(\cdot)$ denotes the n-th order Bessel function of the first kind. Note that Eq. (6) inherently satisfies the traction-free condition on the ground surface (2).

The total scattered field u^S in the open region 1 may be separated into two parts, u^{S1} and u^{S2}. Thus,

$$u^S(r,\theta) = u^{S1}(r,\theta) + u^{S2}(r,\theta). \tag{7}$$

The first component u^{S1} represents the scattered field without the effect of region 2. We may regard u^{S1} as the scattered field induced by a semicircular canyon,

$$u^{S1}(r,\theta) = \sum_{n=0}^{\infty} \tilde{A}_n \frac{H_{2n}^{(2)}(kr)}{H_{2n}^{(2)'}(ka)} \cos(2n\theta) + \sum_{n=0}^{\infty} \tilde{B}_n \frac{H_{2n+1}^{(2)}(kr)}{H_{2n+1}^{(2)'}(ka)} \sin[(2n+1)\theta], \tag{8}$$

where $H_n^{(2)}(\cdot)$ is the n-th order Hankel function of the second kind, and the primes stand for differentiation with respect to the arguments of corresponding functions. Following the derivation given by Trifunac [2] for plane-wave incidence, we derive a line-source version for the scattered coefficients $\tilde{A}_n$ and $\tilde{B}_n$, whose exact analytical expressions are as follows:

$$\tilde{A}_n = -2\varepsilon_n \frac{H_{2n}^{(2)}(kr_s)}{H_0^{(2)}(kr_s)} \cos(2n\theta_s) J_{2n}'(ka), \tag{9}$$

$$\tilde{B}_n = -4 \frac{H_{2n+1}^{(2)}(kr_s)}{H_0^{(2)}(kr_s)} \sin[(2n+1)\theta_s] J_{2n+1}'(ka). \tag{10}$$

The second component u^{S2} indicates the scattered field induced by the existence of region 2. Following Eq. (8), we may write

$$u^{S2}(r,\theta) = \sum_{n=0}^{\infty} A_n \frac{H_{2n}^{(2)}(kr)}{H_{2n}^{(2)'}(ka)} \cos(2n\theta) + \sum_{n=0}^{\infty} B_n \frac{H_{2n+1}^{(2)}(kr)}{H_{2n+1}^{(2)'}(ka)} \sin[(2n+1)\theta], \tag{11}$$

where the complex expansion coefficients A_n and B_n are unknown. Actually, Eq. (11) can be viewed as a correction term to Eq. (8).

In region 1, the resultant wavefield displacement u_1, that is composed of the free wavefield and the total scattered wavefield, is given by

$$u_1(r,\theta) = u^F(r,\theta) + u^S(r,\theta). \tag{12}$$

In region 2, the wavefield displacement u_2 that satisfies Eq. (1) without the forcing term and Eq. (4) may be expressed as

$$u_2(r_1,\theta_1) = \sum_{n=0}^{\infty} C_n \frac{J_{2n}(kr_1)}{J_{2n}'(ka)} \cos(2n\theta_1) + \sum_{n=0}^{\infty} D_n \frac{J_{2n+1}(kr_1)}{J_{2n+1}'(ka)} \sin[(2n+1)\theta_1], \tag{13}$$

where the complex expansion coefficients C_n and D_n will be determined later.

2.2 Coordinate transformation

Before imposing the matching conditions on S_a, the two distinct polar coordinate systems in regions 1 and 2 have to be unified. This is a key step of the solution process. In order to rewrite Eq. (13) in terms of (r, θ), the necessary coordinate transformation from (r_1, θ_1) to (r, θ) is made via Graf's addition formula for Bessel functions (see [70]), which is recast in an appropriate form as follows:

$$J_n(kr_1)\left\{\begin{matrix}\cos n\theta_1\\ \sin n\theta_1\end{matrix}\right\} = (-1)^n \sum_{m=0}^{\infty} J_m(kr)\left\{\begin{matrix}J^+_{m,n}\cos m\theta\\ J^-_{m,n}\sin m\theta\end{matrix}\right\}, \tag{14}$$

where

$$J^{\pm}_{m,n} = \frac{\varepsilon_m}{2}\left[(-1)^n J_{m-n}(kd) \pm J_{m+n}(kd)\right]. \tag{15}$$

Substituting Eq. (14) into (13) results in

$$u_2(r,\theta) = \sum_{n=0}^{\infty}\frac{C_n}{J'_{2n}(ka)}\sum_{m=0}^{\infty} J_m(kr)J^+_{m,2n}\cos m\theta - \sum_{n=0}^{\infty}\frac{D_n}{J'_{2n+1}(ka)}\sum_{m=1}^{\infty} J_m(kr)J^-_{m,2n+1}\sin m\theta. \tag{16}$$

2.3 Determination of expansion coefficients

Taking into account the stress continuity condition on S_a, we have

$$\tau^{(1)}_{rz}(r,\theta) = \tau^{(2)}_{rz}(r,\theta), \quad -\beta \le \theta \le \beta, \quad r = a. \tag{17}$$

Multiplying Eq. (17) by a sequence of cosine/sine functions and integrating over the appropriate intervals leads to

$$\int_{-\pi/2}^{\pi/2}\frac{\partial u_1(a,\theta)}{\partial r}\cos(2q\theta)\,\mathrm{d}\theta = \int_{-\beta}^{\beta}\frac{\partial u_2(a,\theta)}{\partial r}\cos(2q\theta)\,\mathrm{d}\theta, \quad q = 0, 1, \ldots, \tag{18}$$

$$\int_{-\pi/2}^{\pi/2}\frac{\partial u_1(a,\theta)}{\partial r}\sin\left[(2q+1)\theta\right]\mathrm{d}\theta = \int_{-\beta}^{\beta}\frac{\partial u_2(a,\theta)}{\partial r}\sin\left[(2q+1)\theta\right]\mathrm{d}\theta, \quad q = 0, 1, \ldots. \tag{19}$$

Exploiting the orthogonal property, the following relations hold:

$$A_n = \frac{\varepsilon_n}{\pi}\sum_{p=0}^{\infty}\frac{C_p}{J'_{2p}(ka)}\sum_{m=0}^{\infty} J'_m(ka)J^+_{m,2p}I^C_{m,2n}, \tag{20}$$

$$B_n = -\frac{2}{\pi}\sum_{p=0}^{\infty}\frac{D_p}{J'_{2p+1}(ka)}\sum_{m=1}^{\infty} J'_m(ka)J^-_{m,2p+1}I^S_{m,2n+1}, \tag{21}$$

where

$$I^C_{m,n} = \begin{cases} 2\beta, & m = n = 0,\\ \beta + \frac{\sin(2n\beta)}{2n}, & m = n \neq 0,\\ 2\frac{m\cos(n\beta)\sin(m\beta) - n\cos(m\beta)\sin(n\beta)}{m^2-n^2}, & m \neq n,\end{cases} \tag{22}$$

$$I^S_{m,n} = \begin{cases} \beta - \frac{\sin(2n\beta)}{2n}, & m = n,\\ 2\frac{n\cos(n\beta)\sin(m\beta) - m\cos(m\beta)\sin(n\beta)}{m^2-n^2}, & m \neq n.\end{cases} \tag{23}$$

Likewise, enforcing the displacement continuity across S_a,

$$u_1(r,\theta) = u_2(r,\theta), \quad -\beta \le \theta \le \beta, \quad r = a, \tag{24}$$

applying a succession of cosine functions, and integrating over the range $[-\beta, \beta]$ gives

$$\int_{-\beta}^{\beta} u_1(a,\theta)\cos(2q\theta)\,\mathrm{d}\theta = \int_{-\beta}^{\beta} u_2(a,\theta)\cos(2q\theta)\,\mathrm{d}\theta, \quad q = 0, 1, \ldots. \tag{25}$$

Applying Eq. (20) to eliminate the scattering coefficients A_n, using the Wronskian relations for Bessel and Hankel functions (e.g. [71], pp. 113, Eq. 5.9.3), and rearranging, we get a system of linear algebraic equations with unknown coefficients C_n,

$$\sum_{n=0}^{\infty} C_n L^C_{q,n} = R^C_q, \quad q = 0, 1, \ldots, \tag{26}$$

where the pertinent functions used for brevity are shown in Appendix A (see Eqs. A1 and A2).

Similarly, multiplying Eq. (24) by a chain of sine functions yields

$$\int_{-\beta}^{\beta} u_1(a,\theta)\sin[(2q+1)\theta]\,\mathrm{d}\theta = \int_{-\beta}^{\beta} u_2(a,\theta)\sin[(2q+1)\theta]\,\mathrm{d}\theta, \quad q = 0, 1, \ldots. \tag{27}$$

Accordingly, we arrive at another system of linear algebraic equations:

$$\sum_{n=0}^{\infty} D_n L^S_{q,n} = R^S_q, \quad q = 0, 1, \ldots, \tag{28}$$

where the detailed expressions are given in Appendix A (see Eqs. A3 and A4).

For numerical computations, it is necessary to truncate the infinite series of Eqs. (26) and (28) to a finite number of terms. The expansion coefficients C_n and D_n may be evaluated by standard matrix techniques. In Eqs. (26) and (28), the summation indices n and weighting indices q are truncated after $N-1$ terms. Therefore, Eqs. (26) and (28) constitute a system of N equations with N unknowns, respectively. The number of truncation terms in consideration depends only on the requirement of accuracy. Once the coefficients C_n and D_n are found, the expansion coefficients A_n and B_n may be evaluated straightforwardly via Eqs. (20) and (21).

3 Results and discussions

The displacement amplitude $|u|$ at a specific location in the region concerned is given by

$$|u| = \begin{cases} |u_1| = \sqrt{[\mathrm{Re}(u_1)]^2 + [\mathrm{Im}(u_1)]^2} & \text{for region 1,} \\ |u_2| = \sqrt{[\mathrm{Re}(u_2)]^2 + [\mathrm{Im}(u_2)]^2} & \text{for region 2.} \end{cases} \tag{29}$$

The dimensionless frequency η is defined as

$$\eta = \frac{ka}{\pi} = \frac{2a}{\lambda}, \tag{30}$$

in which λ is the excitation wavelength.

Before turning to parametric analysis, the determination of the appropriate truncation value N in Eqs. (26) and (28) is necessary. It is worth emphasizing that the series with indices m (see Eqs. A1 and A3 in Appendix A)

are truncated to M terms. To get rid of the problem regarding relative convergence, the inner sums with indices m should be checked carefully, thereby leaving only one parameter (i.e. indices n for outer sums). The process of checking the truncation value M involves successive computations for the surface displacement amplitudes $|u|$ against the dimensionless horizontal distance x/a, calculated from $M = 10$ to 400 with the interval of 10. The maximum values of relative errors are evaluated from the displacement amplitudes at 800 equally spaced locations, ranging between $x/a = -4$ and 4. The convergence criterion for M is that the maximum relative error falls below the threshold value of $10^{-10}\%$. Following extensive numerical experiments, the value of $M = 200$ is adequate to produce all the graphs hereafter. Similarly, the same checking procedure is applied to obtain the suitable truncation value N. Generally, a rise in excitation frequency increases the value of N.

3.1 Validation

Since there are no similar results available in the existing literature, a computer program based on the classical boundary-element method (BEM) is utilized for validation. The results are computed for both the analytical expressions and the BEM solution. Figure 2 gives the computed results of $|u|$ versus x/a. Figure 2a illustrates the case of the deep canyon of $d/a = 0.7$ subjected to an on-axis source at $r_s/a = 2$ and $\theta_s = 0°$ with $\eta = 4$. Figure 2b shows the shallow canyon of $d/a = 0.3$ subjected to an off-axis source at $r_s/a = 1.5$ and $\theta_s = 45°$ with $\eta = 2$. The abscissa ranges from $x/a = -4$ to 4. A bold black line displays the locations within canyon site (from $x/a = -1$ to 1). From Figure 2a and b, one can find that these results show a reasonably good quantitative agreement. This confirms the validity of Eqs. (6)–(16), (20)–(23), (26), and (28) shown in Sect. 2. In following subsections, only the theoretical series expansion solution is plotted, not the BEM.

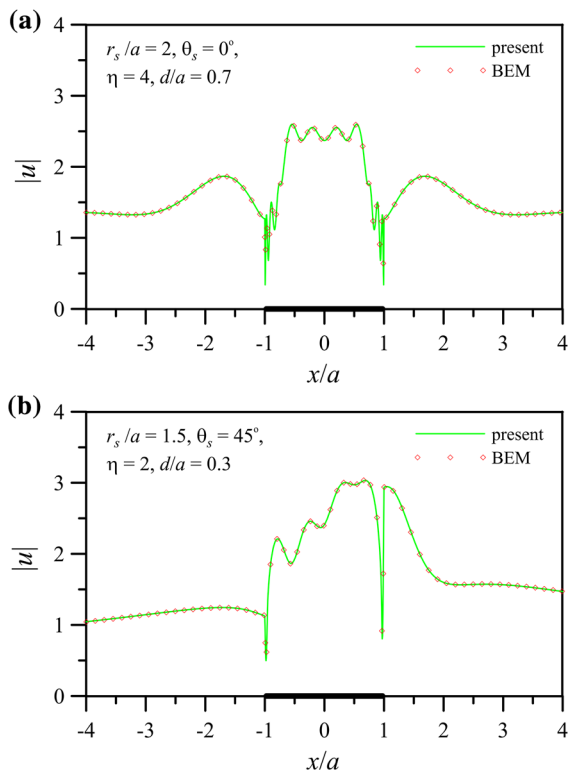

Fig. 2 Surface displacement amplitude versus x/a: **a** on-axis source with $\eta = 4$ for $d/a = 0.7$; **b** off-axis source with $\eta = 2$ for $d/a = 0.3$. Solid green lines display the results of the theoretical series solution (given by Eqs. 12 and 13), while hollow red rhombuses show those obtained by the BEM

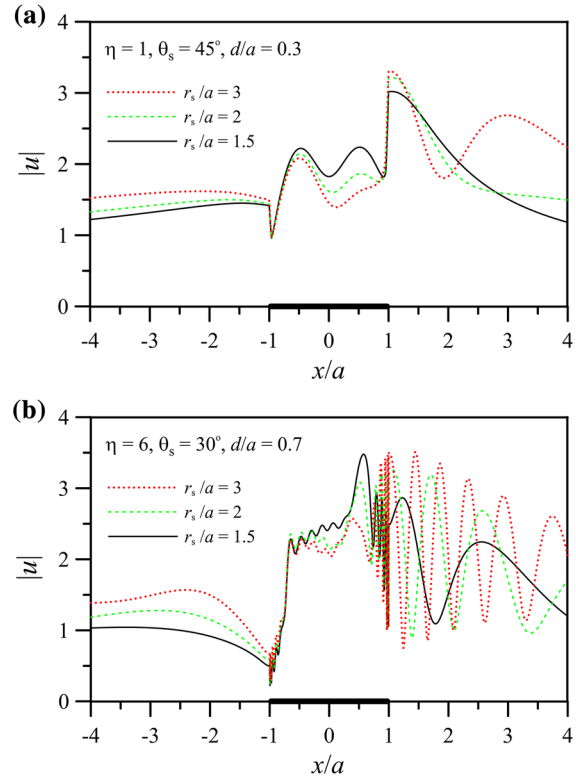

Fig. 3 Surface displacement amplitude versus x/a for different source distances: **a** $\theta_s = 45°$, $\eta = 1$ and $d/a = 0.3$; **b** $\theta_s = 30°$, $\eta = 6$ and $d/a = 0.7$

3.2 Frequency-domain motions

In order to demonstrate the impact of source distance on surface motions, Fig. 3 features the computed results for $r_s/a = 1.5$, 2, and 3: Fig. 3a for $\theta_s = 45°$, $\eta = 1$ and $d/a = 0.3$, and Fig. 3b for $\theta_s = 30°$, $\eta = 6$ and $d/a = 0.7$. As observed in Fig. 3a and b, the amplitudes of motions on the left-hand horizontal ground surface (i.e. $x/a \leq -1$) increase when the value of source distance rises. Similar trend may be found for the peak values of motions on the right-hand horizontal ground surface close to the upper right corner of the canyon (about $1 \leq x/a \leq 1.3$). However, the displacement amplitudes at the bottom of the canyon decrease with increasing r_s/a (see about $-0.5 \leq x/a \leq 0.8$ in Fig. 3a and about $-0.3 \leq x/a \leq 0.7$ in Fig. 3b).

In the high-frequency case (see Fig. 3b), some extreme oscillation to the right of the canyon particularly for $r_s/a = 3$ can be found. Such an oscillatory behaviour may be attributed to two main reasons. Firstly, more parts of the wavefront of the off-axis source hit the upper right corner area (cf. Fig. 7b) when the value of r_s/a becomes larger. This implies that more standing waves through constructive interference occur near the right-angled area (i.e. $x/a = 1$). Secondly, with higher frequencies, more standing waves are possible. This also leads to an oscillatory trait of displacement amplitudes, which is evident in the later diagram (see Fig. 5b).

Typical simulation results for different source angles ($\theta_s = 15°$, 30°, and 45°) are presented in Fig. 4: Fig. 4a for $r_s/a = 1.5$, $\eta = 0.5$ and $d/a = 0.3$, and Fig. 4b for $r_s/a = 2$, $\eta = 2$ and $d/a = 0.5$. Both Fig. 4a and b reveal that the shielding effect of the canyon becomes more apparent when the seismic source moves gradually towards the horizontal ground surface. See an overall decreasing trend in displacement amplitudes on the left-hand horizontal ground surface. Furthermore, the peak amplitudes of motions in the range of $1 < x/a < 1.5$ shift upward as θ_s increases. This may be primarily because of geometric focusing occurring near the upper right corner of the canyon. Besides, in Fig. 4b, some extreme dips around the two upper corners of the canyon can be observed. The existence of pronounced and sharp dips can be also found in Figs. 2a, b, 3b, 5a, and b. Such a localized de-amplification effect on displacement amplitudes may be due to destructive interference between the reflected waves (from the

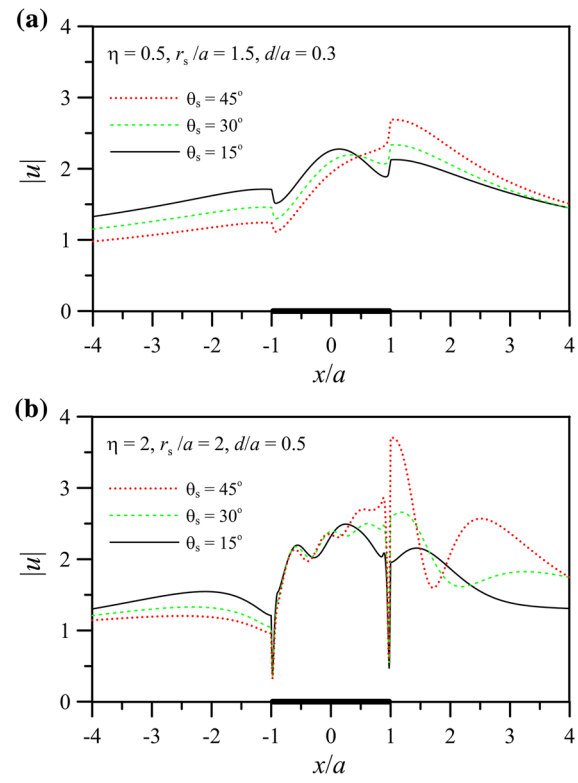

Fig. 4 Surface displacement amplitude versus x/a for different source angles: **a** $r_s/a = 1.5$, $\eta = 0.5$ and $d/a = 0.3$; **b** $r_s/a = 2$, $\eta = 2$ and $d/a = 0.5$

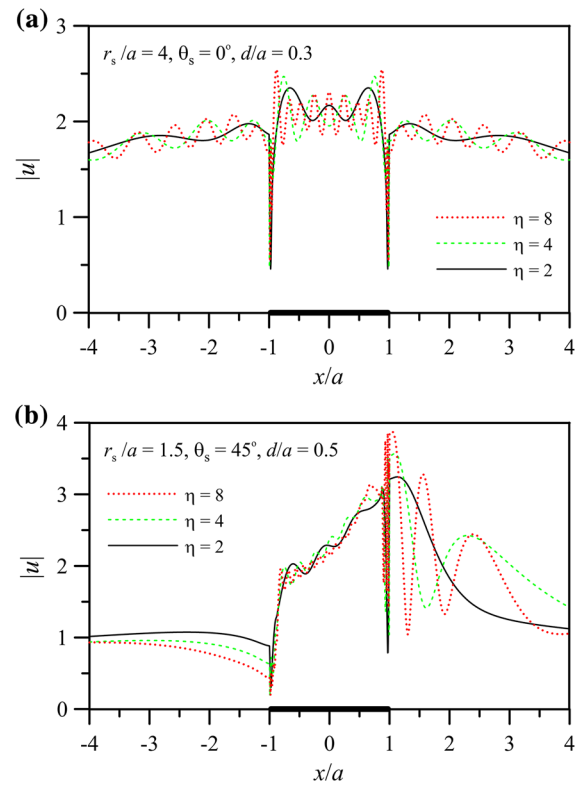

Fig. 5 Surface displacement amplitude versus x/a for different dimensionless frequencies: **a** $r_s/a = 4$, $\theta_s = 0°$ and $d/a = 0.3$; **b** $r_s/a = 1.5$, $\theta_s = 45°$ and $d/a = 0.5$

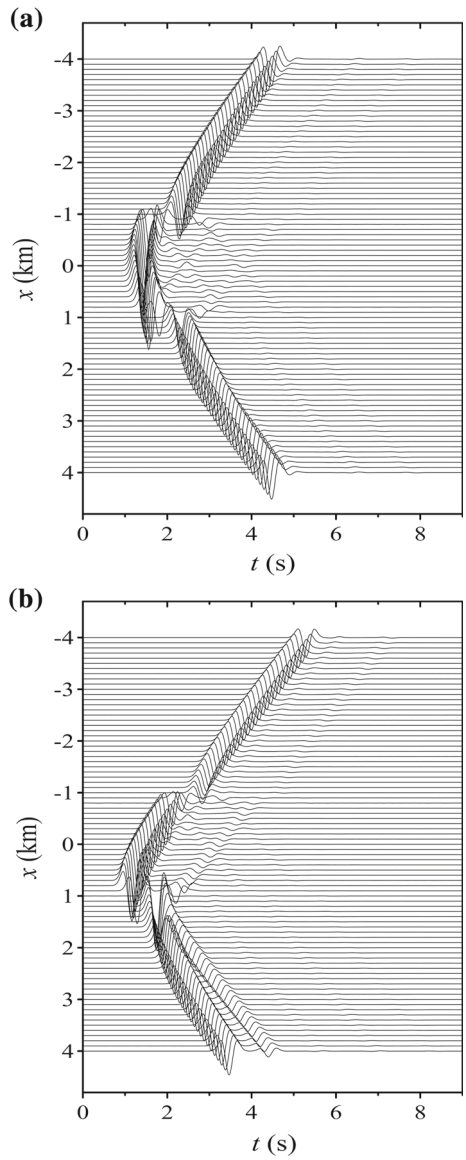

Fig. 6 Synthetic seismograms for the canyon with $d/a = 0.6$ subjected to incident SH pulses with $f_c = 2$ Hz and $r_s/a = 2$: **a** $\theta_s = 0°$; **b** $\theta_s = 30°$

canyon face and the horizontal ground surface) and the direct waves. This phenomenon is quite obvious when the characteristic length of the canyon is greater than two times the wavelength of excitation source (i.e. $\eta \geq 2$).

The results for different dimensionless frequencies ($\eta = 2$, 4, and 8) are plotted in Fig. 5: Fig. 5a for $r_s/a = 4$, $\theta_s = 0°$ and $d/a = 0.3$, and Fig. 5b for $r_s/a = 1.5$, $\theta_s = 45°$ and $d/a = 0.5$. As shown in Fig. 5a and b, the fluctuation of surface motions in the illuminated area becomes more oscillatory as η increases. For the case of on-axis source, the patterns of displacement amplitudes are symmetric about the central axis of the canyon, as expected due to geometric symmetry of the canyon (see Fig. 5a).

3.3 Time-domain motions

Transient response of the present concave topography may be simulated via the inverse fast Fourier transform. The symmetric Ricker wavelet given by

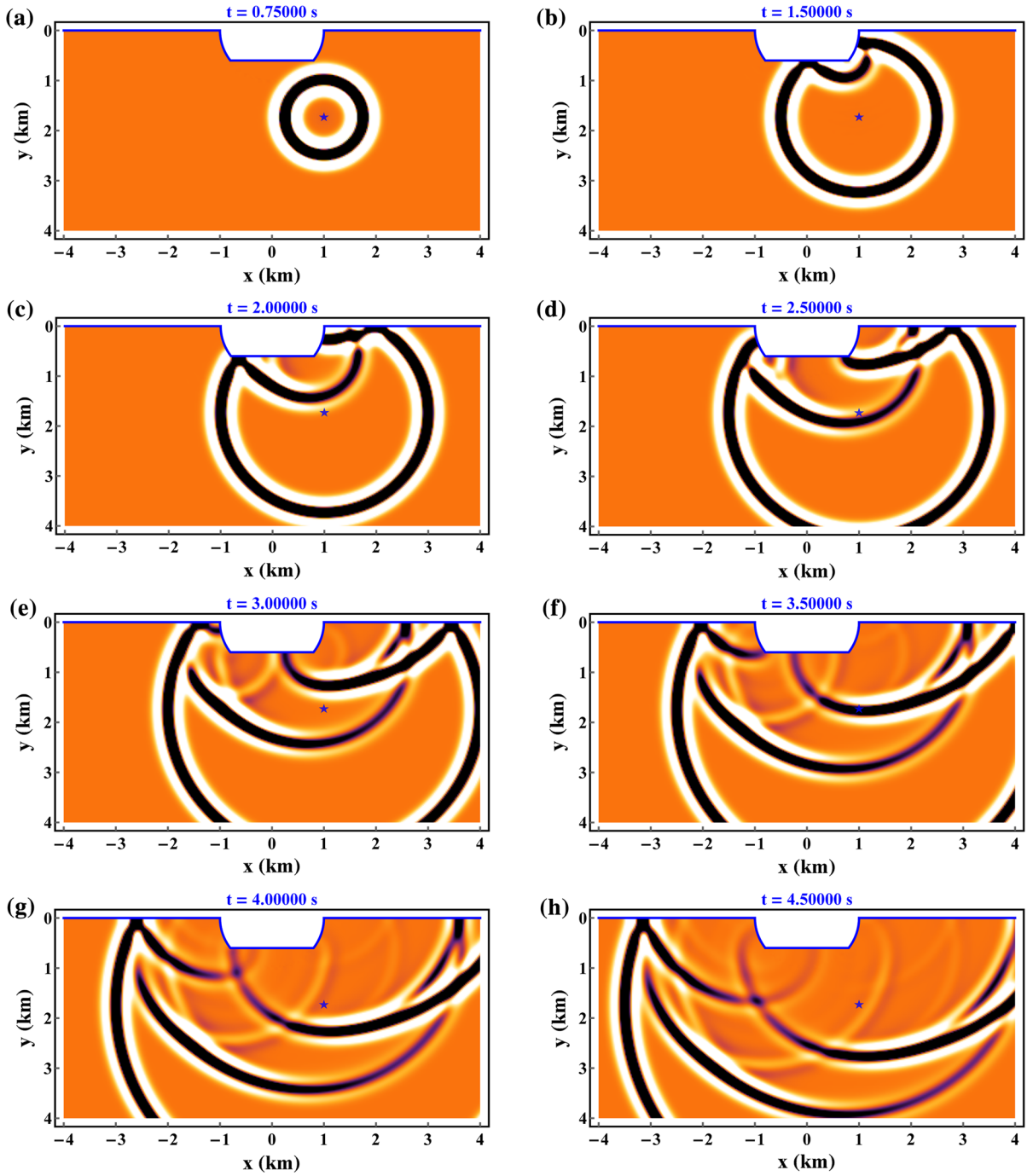

Fig. 7 Snapshots of subsurface displacements around the canyon with $d/a = 0.6$ subjected to incident SH pulses with $f_c = 2$ Hz, $r_s/a = 2$ and $\theta_s = 30°$

$$u(t) = (2\pi^2 f_c^2 t^2 - 1)\exp(-\pi^2 f_c^2 t^2) \tag{31}$$

is adopted as the source time function with characteristic frequency f_c. The canyon with $d/a = 0.6$ is selected as the targeted site. The half-width of the canyon top is taken as 1 km. The shear-wave velocity of the semi-infinite

medium is 1 km/s. The frequency-domain results evaluated for $f_c = 2$ Hz range between 0.0625 and 8 Hz. The frequency increment is set to 0.0625 Hz, corresponding to a forecasting time window of 16 s.

The theoretically predicted synthetic seismograms are given in Fig. 6: Fig. 6a for an on-axis source at $r_s/a = 2$ and $\theta_s = 0°$, and Fig. 6b for an off-axis source at $r_s/a = 2$ and $\theta_s = 30°$. The simulated ground-motion time histories are taken from eighty-one equispaced seismometers situated between $x = -4$ and 4 km. As shown in Fig. 6a and b, several reflected and scattered wave signals may be clearly detected after the direct-wave signals. For receivers close to the two upper corners of the canyon ($x = \pm 1$ km), the de-amplified signals attributed to the shielding effect of the canyon are evident, as well as the amplified signals due to geometric focusing (see Fig. 6b).

For the sake of clearly identifying the causes of displacement waveforms displayed in Fig. 6b, the snapshots of the spatial distribution of underground motions at eight different representative times are shown in Fig. 7. As expected, the two wavefronts spreading outwards from the two lower corners of the canyon meet each other and eventually dissipates at much later times (see also X-shaped patterns in Fig. 6b).

4 Conclusions

We have improved the 2-D simplified canyon model previously proposed by Tsaur and Chang [11] and extended it to explore ground-motion variability induced by the joint effects of near-field source and surface topography. The forward elastodynamic problem for a specific scatterer considered herein has been solved by the RMT. Displacement responses in each frequency-domain case were in good agreement with the results generated from BEM simulations. The theoretical modelling indicates that the phenomenon of geometric focusing of seismic wavefields near the two upper corners of the canyon may bring about potential amplification of ground motions. In future 2-D modelling going forward, we may wish to consider the effects of attenuation and stacked layered materials.

Acknowledgements K.-H.C. and S.-C.H. are sincerely grateful for the financial support granted by the Ministry of Science and Technology, Taiwan, Republic of China (Project Nos. MOST 103-2218-E-033-005 and MOST 104-2221-E-033-036). Special thanks goes to Prof. Deng-How Tsaur for kindly providing an in-house BEM program developed in Wave Mechanics Lab at National Taiwan Ocean University.

Appendix A: Pertinent functions in Eqs. (26) and (28)

In Eqs. (26) and (28), the associated functions are listed as follows:

$$L^C_{q,n} = \sum_{m=0}^{\infty} \frac{J^+_{m,2n}}{J'_{2n}(ka)} \sum_{p=0}^{\infty} \left[\frac{\varepsilon_p J'_m(ka)}{\pi} \frac{H^{(2)}_{2p}(ka)}{H^{(2)'}_{2p}(ka)} I^C_{m,2p} I^C_{2p,2q} \delta_{p,q} J_m(ka) I^C_{m,2q} \right], \tag{A1}$$

$$R^C_q = \frac{4i}{\pi a} \sum_{n=0}^{\infty} \varepsilon_n \frac{H^{(2)}_{2n}(kr_s)}{H^{(2)}_0(kr_s)} \frac{\cos(2n\theta_s)}{H^{(2)'}_{2n}(ka)} I^C_{2n,2q}, \tag{A2}$$

$$L^S_{q,n} = \sum_{m=1}^{\infty} \frac{J^-_{m,2n+1}}{J'_{2n+1}(ka)} \sum_{p=0}^{\infty} \left[\frac{2J'_m(ka)}{\pi} \frac{H^{(2)}_{2p+1}(ka)}{H^{(2)'}_{2p+1}(ka)} I^S_{m,2p+1} I^S_{2p+1,2q+1} \delta_{p,q} J_m(ka) I^S_{m,2q+1} \right], \tag{A3}$$

$$R^S_q = -\frac{8i}{\pi a} \sum_{n=0}^{\infty} \frac{H^{(2)}_{2n+1}(kr_s)}{H^{(2)}_0(kr_s)} \frac{\sin[(2n+1)\theta_s]}{H^{(2)'}_{2n+1}(ka)} I^S_{2n+1,2q+1}. \tag{A4}$$

References

1. Massa M, Barani S, Lovati S (2014) Overview of topographic effects based on experimental observations: meaning, causes and possible interpretations. Geophys J Int 197(3):1537–1550

2. Trifunac MD (1973) Scattering of plane SH waves by a semi-cylindrical canyon. Earthq Eng Struct Dyn 1(3):267–281
3. Wong HL, Trifunac MD (1974) Scattering of plane SH waves by a semi-elliptical canyon. Earthq Eng Struct Dyn 3(2):157–169
4. Chang KH, Tsaur DH, Wang JH (2013) Scattering of SH waves by a circular sectorial canyon. Geophys J Int 195(1):532–543
5. Chang KH, Tsaur DH, Wang JH (2014) Ground motions around a semi-circular valley partially filled with an inclined alluvial layer under SH-polarized excitation. Earth Planets Space 66(1):53
6. Chang KH, Tsaur DH, Wang JH (2016) Ground motions around a semicircular canyon with a dipping edge under SH plane wave incidence. J Seismol 20(1):117–136
7. Tsaur DH, Chang KH (2008) SH-waves scattering from a partially-filled semi-circular alluvial valley. Geophys J Int 173(1):157–167
8. Tsaur DH, Chang KH (2009) Scattering and focusing of SH waves by a convex circular-arc topography. Geophys J Int 177(1):222–234
9. Tsaur DH, Chang KH (2012) Multiple scattering of SH waves by an embedded truncated circular cavity. J Mar Sci Technol 20(1):73–81
10. Tsaur DH, Chang KH, Hsu MS (2010) An analytical approach for the scattering of SH waves by a symmetrical Vshaped canyon: deep case. Geophys J Int 183(3):1501–1511
11. Tsaur DH, Chang KH (2009) Scattering of SH waves by truncated semicircular canyon. J Eng Mech ASCE 135(8):862–870
12. Hsu MS, Tsaur DH (2014) Scattering of SH waves by a truncated semi-elliptic canyon. J Mech 30(2):137–144
13. Chang KH, Tsaur DH, Wang JH (2015) Response of a shallow asymmetric V-shaped canyon to antiplane elastic waves. Proc R Soc A 471(2174):20140215
14. Tsaur DH, Chang KH (2008) An analytical approach for the scattering of SH waves by a symmetrical V-shaped canyon: shallow case. Geophys J Int 174(1):255–264
15. Zhang C, Liu Q, Deng P (2015) Antiplane scattering of SH waves by a trapezoidal valley with a circular-arc alluvium in an elastic half space. J Earthq Tsunami 9(3):1550008
16. Balendra T, Thambiratnam DP, Koh CG, Lee SL (1984) Dynamic response of twin circular tunnels due to incident SH-waves. Earthq Eng Struct Dyn 12(2):181–201
17. Kara HF (2016) A note on response of tunnels to incident SH-waves near hillsides. Soil Dyn Earthq Eng 90:138–146
18. Lee VW (1977) On deformations near circular underground cavity subjected to incident plane SH waves. In: Proceeding of the applications of computer methods in engineering conference, pp 951–962
19. Li BL, Fang XQ, Yuan RJ (2019) Predicting the crack open displacements of a partially debonded pipeline in rock mass under SH waves. Eng Fail Anal 96:80–87
20. Liu Q, Zhang C, Todorovska MI (2016) Scattering of SH waves by a shallow rectangular cavity in an elastic half space. Soil Dyn Earthq Eng 90:147–157
21. Liu Q, Wu Z, Lee VW (2019) Scattering and reflection of SH waves around a slope on an elastic wedged space. Earthq Eng Eng Vib 18(2):255–266
22. Liu Q, Zhao M, Liu Z (2019) Wave function expansion method for the scattering of SH waves by two symmetrical circular cavities in two bonded exponentially graded half spaces. Eng Anal Bound Elem 106:389–396
23. Luo H, Lee VW, Liang J (2010) Anti-plane (SH) waves diffraction by an underground semi-circular cavity: analytical solution. Earthq Eng Eng Vib 9(3):385–396
24. Sánchez-Sesma FJ (1985) Diffraction of elastic SH waves by wedges. Bull Seism Soc Am 75(5):1435–1446
25. Trifunac MD (1971) Surface motion of a semi-cylindrical alluvial valley for incident plane SH waves. Bull Seismol Soc Am 61(6):1755–1770
26. Tsaur DH (2010) Exact scattering and diffraction of antiplane shear waves by a vertical edge crack. Geophys J Int 181(3):1655–1664
27. Tsaur DH (2011) Scattering and focusing of SH waves by a lower semielliptic convex topography. Bull Seismol Soc Am 101(5):2212–2219
28. Tsaur DH, Chang KH (2018) Exact solution to scattering of SH waves by an elliptic-arc canyon in the corner of an elastic quarter space. Soil Dyn Earthq Eng 110:137–140
29. Wong HL, Trifunac MD (1974) Surface motion of a semi-elliptical alluvial valley for incident plane SH waves. Bull Seism Soc Am 64(5):1389–1408
30. Ba Z, Yin X (2016) Wave scattering of complex local site in a layered half-space by using a multidomain IBEM: incident plane SH waves. Geophys J Int 205(3):1382–1405
31. Ducellier A, Aochi H (2012) Interactions between topographic irregularities and seismic ground motion investigated using a hybrid FD-FE method. Bull Earthq Eng 10(3):773–792
32. Kawase H (1988) Time-domain response of a semi-circular canyon for incident SV, P and Rayleigh waves calculated by the discrete wavenumber boundary element method. Bull Seism Soc Am 78(4):1415–1437
33. Komatitsch D, Vilotte JP (1998) The spectral element method: an efficient tool to simulate the seismic response of 2D and 3D geological structures. Bull Seism Soc Am 88(2):368–392
34. Moczo P, Kristek J, Galis M, Pazak P, Balazovjech M (2007) The finite-difference and finite-element modeling of seismic wave propagation and earthquake motion. Acta Phys. Slovaca 57(2):177–406
35. Nohegoo-Shahvari A, Kamalian M, Panji M (2019) A hybrid time-domain half-plane FE/BE approach for SH-wave scattering of alluvial sites. Eng Anal Bound Elements 105:194–206
36. Tang Z, Fu Z, Zhang D, Huang J (2018) Singular boundary method to simulate scattering of SH wave by the canyon topography. Adv Appl Math Mech 10(4):912–924

37. Ba Z, Wang Y, Liang J, Liu X (2019) 3D dynamic responses of a 2D hill in a layered half-space subjected to obliquely incident plane P-, SV- and SH-waves. Eng Anal Bound Elem 105:129–145
38. Glinsky N, Bertrand E, Régnier J (2019) Numerical simulation of topographical and geological site effects. Applications to canonical topographies and Rognes hill, South East France. Soil Dyn Earthq Eng 116:620–636
39. Lovati S, Bakavoli MKH, Massa M, Ferretti G, Pacor F, Paolucci R, Haghshenas E, Kamalian M (2011) Estimation of topographical effects at Narni ridge (Central Italy): comparisons between experimental results and numerical modelling. Bull Earthq Eng 9:1987–2005
40. Poursartip B, Fathi A, Kallivokas LF (2017) Seismic wave amplification by topographic features: a parametric study. Soil Dyn Earthq Eng 92:503–527
41. Sills LB (1978) Scattering of horizontally-polarized shear waves by surface irregularities. Geophys J R Astr Soc 54(2):319–348
42. Takemiya H, Fujiwara A (1994) SH-wave scattering and propagation analysis at irregular sites by time domain BEM. Bull Seism Soc Am 84(5):1443–1455
43. Datta SK, Shah AH (1982) Scattering of SH waves by embedded cavities. Wave Motion 4(3):265–283
44. Fontara IK, Dineva PS, Manolis GD, Wuttke F (2016) Numerical simulation of seismic wave field in graded geological media containing multiple cavities. Geophys J Int 206(2):921–940
45. Li ZL, Li JC, Li X (2019) Seismic interaction between a semi-cylindrical hill and a nearby underground cavity under plane SH waves. Geomech Geophys Geo-energy Geo-resour 5:405–423
46. Lu JF, Hanyga A (2004) Dynamic interaction between multiple cracks and a circular hole swept by SH waves. Int J Solids Struct 41:6725–6744
47. Luco JE, de Barros FCP (1994) Dynamic displacements and stresses in the vicinity of a cylindrical cavity embedded in a half-space. Earthq Eng Struct Dyn 23(3):321–340
48. Panji M, Kamalian M, Asgari Marnani J, Jafari MK (2013) Transient analysis of wave propagation problems by half-plane BEM. Geophys J Int 194(3):1849–1865
49. Panji M, Mojtabazadeh-Hasanlouei S, Yasemi F (2020) A half-plane time-domain BEM for SH-wave scattering by a subsurface inclusion. Comput Geosci 134:104342
50. Yu CW, Dravinski M (2009) Scattering of a plane harmonic SH wave by a completely embedded corrugated scatterer. Int J Numer Methods Eng 78(2):196–214
51. Gal M, Reading AM, Rawlinson N, Schulte-Pelkum V (2018) Matched field processing of three-component seismic array data applied to Rayleigh and Love microseisms. J Geophys Res Solid Earth 123(8):6871–6889
52. Maxwell S (2014) Microseismic imaging of hydraulic fracturing: improved engineering of unconventional shale reservoirs. SEG distinguished instructor series no. 17, Tulsa, US
53. Moniri H (2017) Evaluation of seismic performance of reinforced concrete (RC) buildings under near-field earthquakes. Int J Adv Struct Eng 9(1):13–25
54. Hall JF, Heaton TH, Halling MW, Wald DJ (1995) Near-source ground motion and its effects on flexible buildings. Earthq Spectra 11(4):569–605
55. Sunasaka Y, Toki K, Kiremidjian AS (2003) Evaluation of damage potential of ground motions during great earthquakes. Earthq Spectra 19(3):713–730
56. Groby JP, Wirgin A (2008) Seismic motion in urban sites consisting of blocks in welded contact with a soft layer overlying a hard half-space. Geophys J Int 172(2):725–758
57. Jalali RS, Tokmechi Z (2016) A note on the surface motion of a semi-cylindrical canyon for incident cylindrical SH waves radiated by a finite fault. Earthq Eng Eng Vib 15(3):445–455
58. Groby JP, Wirgin A (2005a) Two-dimensional ground motion at a soft viscoelastic layer/hard substratum site in response to SH cylindrical seismic waves radiated by deep and shallow line sources–I. Theory. Geophys J Int 163(1):165–191
59. Groby JP, Wirgin A (2005b) Two-dimensional ground motion at a soft viscoelastic layer/hard substratum site in response to SH cylindrical seismic waves radiated by deep and shallow line sources–II. Numerical results. Geophys J Int 163(1):192–224
60. Jalali RS, Tokmechi Z, Trifunac MD (2015) A note on the surface motion of a semi-cylindrical alluvial valley for incident-cylindrical SH waves radiating from a fault with arbitrary orientation. Soil Dyn Earthq Eng 79:80–88
61. Zhang N, Gao Y, Wu Y, Zhang F (2018) A note on near-field site amplification effects of ground motion from a radially inhomogeneous valley. Earthq Eng Eng Vib 17(4):707–718
62. Gao Y, Dai D, Zhang N, Wu Y, Mahfouz AH (2017) Scattering of plane and cylindrical SH waves by a horseshoe shaped cavity. J Earthq Tsunami 11(2):1650011
63. Smerzini C, Avilés J, Paolucci R, Sánchez-Sesma FJ (2009) Effect of underground cavities on surface earthquake ground motion under SH wave propagation. Earthq Eng Struct Dyn 38(12):1441–1460
64. Valencia C, Gomez J, Jaramillo J, Saenz M, Vergara J (2017) The scattering of SH waves by a finite crack with a superposition-based diffraction technique. Stud Geophys Geod 61(1):93–114
65. SánchezSesma FJ, IturraránViveros U (2001) Scattering and diffraction of SH waves by a finite crack: an analytical solution. Geophys J Int 145(3):749–758
66. Gao Y, Zhang N (2013) Scattering of cylindrical SH waves induced by a symmetrical V-shaped canyon: near-source topographic effects. Geophys J Int 193(2):874–885
67. Iturrarán-Viveros U, Vai R, SánchezSesma FJ (2010) Diffraction of SH cylindrical waves by a finite crack: an analytical solution. Geophys J Int 181(3):1634–1642

68. Zhang N, Gao Y, Yang J, Xu C (2015) An analytical solution to the scattering of cylindrical SH waves by a partially filled semi-circular alluvial valley: near-source site effects. Earthq Eng Eng Vib 14(2):189–201
69. Morse PM, Feshbach H (1953) Methods of theoretical physics. Part I. McGraw-Hill, New York
70. Watson GN (1966) A treatise on the theory of Bessel functions, 2nd edn. Cambridge University Press, Cambridge
71. Lebedev NN (1965) Special functions and their applications. In: Silverman RA (ed) Selected Russian publications in the mathematical sciences. Prentice-Hall, Englewood Cliffs, NJ